

Bottom and top reconstruction as benchmarks for the ILD Detector

A. Irles, V. Lohezic, Y. Okugawa, R. Pöschl, F. Richard, H. Yamamoto, R. Yonamine

Abstract

A comprehensive study of bottom-quark pair and top-quark pair production using the semi-leptonic decay channel at $\sqrt{s} = 500$ GeV is presented that benchmark the performance of the current so-called *large* and *small* models of the ILD Detector. The event reconstruction exploits distinguished features of the detector such as lepton identification, vertex charge reconstruction and particle ID with the central TPC of the ILD Detector. With these techniques the final state leptons, the b -quark and \bar{b} -quark and the W can be unambiguously reconstructed. Both detector models perform similarly well with a slight advantage of the large detector model. In case of top quark pair production the selection efficiency is between 30% and 60% for semi-leptonic events. For this channel the note presents an update of the perspective of the physics potential w.r.t. earlier studies for an integrated luminosity of 3200 fb^{-1} . The results for $e^+e^- \rightarrow b\bar{b}$ demonstrate that also this channel can accurately measured at $\sqrt{s} = 500$ GeV.

1. Introduction

Heavy quarks may be messengers of new physics of primary importance [1]. Their large mass compared with other fermions can be explained in Randall Sundrum models [2, 3] featuring warped extra dimensions that are dual to model, which assume that the heavy quarks are composite objects [4]. High precision e^+e^- collisions with polarised beams around the TeV scale are ideally suited to detect new physics effects [5, 6]. Precise measurements of the electroweak couplings of third-generation quarks require superb detector performance in terms of flavour tagging including the event by event determination of the charge of the final state jets to avoid for example migrations in polar angle spectra and/or to reconstruct events in which the heavy quark charge is the only handle to distinguish between particles and anti-particles. The charge determination happens mainly by a combination of the determination of the summed charge of tracks pointing to a secondary vertex or by the identification of the charge of a final state Kaon. This in turn requires a successful particle identification by the detector. Therefore processes with heavy quark final states, i.e. $e^+e^- \rightarrow \phi b\bar{b}$ and $e^+e^- \rightarrow t\bar{t}$ are highly relevant for the benchmarking of the detector performance. In short one can test the following detector capacities.

- Track finding efficiency
- Stringent test of (secondary) vertexing
- Particle ID

In case of $e^+e^- \rightarrow t\bar{t}$ leptonic and semi-leptonic decays of the t -quark pair provide an important additional handle for the accurate measurement of the final state. The analysis presented in this note focuses on the semi-leptonic decay mode of the top-quark pair. The analysis of $t\bar{t}$ production and $b\bar{b}$ production share a number of commonalities. Therefore these two analyses are joined in this note. The analyses presented in this note start out from the PhD thesis of Sviatoslav Bilokin that are based on the DBD samples and software versions [7]. This work has in part been published in Ref [6]. The analyses are ported to the large, IDR-L, and small, IDR-S, detector models, respectively, of the

ILD detector [8] for the International Linear Collider [9]. The research program includes high-statistics running at $\sqrt{s} = 250$ GeV and $\sqrt{s} = 500$ GeV. For further details of the operation scenarios see Ref. [10]. For the process $e^+e^- \rightarrow b\bar{b}$ an analysis at $\sqrt{s} = 500$ GeV is presented instead of $\sqrt{s} = 250$ GeV as in Ref. [6]. The results here benefit from a refined analysis strategy for the ILD paper that is under review in ILD.

2. Methods, tools and Monte Carlo samples

For the event reconstruction we use the **ILCSoft** version **v02-00-02**. The software allows for a full detector simulation and event reconstruction including digitisation steps. For the analyses presented we use the versions **ILD_s5_o1_v02** and **ILD_15_o1_v02** of the detector model.

For the event reconstruction we use the following methods

- ‘Core tools’

- In case of $e^+e^- \rightarrow t\bar{t}$ we use the standard Durham algorithm for jet clustering (**ee_genkt_algorithm** in internal nomenclature) and the Valencia algorithm for $\gamma\gamma$ background removal. Both algorithms are implemented in the **FastJet** package.
- In case of $e^+e^- \rightarrow b\bar{b}$ we use the Valencia jet algorithm implemented in **LCFIPlus** (**ValenciaVertex** in internal nomenclature). We apply the option in which the algorithm does not break secondary vertices. In this algorithm the distance between two objects is calculated as

$$d_{ij} = 2 \min(E_i^{2\beta}, E_j^{2\beta})(1 - \cos \theta_{ij})/R^2 \quad (1)$$

The distance of a particle i to the beam is calculated according to.

$$d_{iB} = E^{2\beta} \sin^{2\gamma} \theta_{iB} \quad (2)$$

The jet algorithm is run with the following settings: $\alpha = \beta = \gamma = 1$, $R = 1.4$

- We use the **LeptonFinder** to identify isolated electrons and muons in semi-leptonic $t\bar{t}$ events.
- For the vertex finding we use the **LCFIPlus** in a private version maintained by Ryo. This version will soon be implemented into the official ILCsoft package.

- Tools developed for the study

- The **VertexRestorer** Processor identifies reconstructed tracks that have not been associated to secondary vertices from B-Meson decays but belongs to this decay according to the Monte Carlo Truth information. It then recovers the ‘lost’ tracks by means of the impact parameters d_0 (transversal) and z_0 (longitudinal). In this present note the recovery uses only the impact parameter d_0 since the algorithms needs to be adapted for the vertex smearing present in the simulation for the IDR.
- The **ParticleTagger** Processor identifies the Kaons by means of the dE/dx measured in the TPC of ILD. It selects a strip in the dE/dx -momentum plane with a high kaon concentration. The efficiency and the purity of the Kaon selection vary as a function of the width of this strip.
- The **QQbarAnalysis** Processor calculates the jet charge and the polar angle of the bottom and top quark pair, respectively. It contains separate methods for the bottom and top quark pair analysis.
- The **TrashRecoProcessor** enables comparisons between reconstructed and generated quantities.

– The described tools are available under <https://github.com/QQbarAnalysis>. This repository contains also a set of macros necessary for the final steps of the analysis.

- The following method combines the results of the two (nearly independent) charge measurements on the b and \bar{b} jet into a robust charge determination.

$$\left. \begin{aligned} N_{acc} &= Np^2 + Nq^2 \\ N_{rej} &= 2Npq \\ 1 &= p + q \end{aligned} \right\} N_{corr} = N_{acc} \cdot \frac{p^2}{p^2 + q^2} \quad (3)$$

where N is total number of events, N_{acc} and N_{rej} are the number of events that were accepted and rejected, respectively. The p and q values represent the probabilities for a correct or an incorrect reconstruction of the b -quark charge, respectively. Solving this equation allows to correct for migrations caused by imperfect reconstruction or $B^0 - \bar{B}^0$ oscillations in the resulting polar angle spectrum. The correction has been applied to the $b\bar{b}$ studies but not (yet) for $t\bar{t}$. For the latter the selection scheme in $t\bar{t}$ is more involved rendering its application less straight forward since e.g. the b -quarks are not necessarily back-to-back.

2.1. Monte Carlo samples

Samples generated with WHIZARD 1.95. Top quark pair production is the dominant process in the $e^+e^- \rightarrow b\bar{b}\ell\nu q\bar{q}$ sample, but it contains also single t and WWZ . In case of the t quark study we have analysed samples for the beam polarisations $\mathcal{P}_{e^-}, \mathcal{P}_{e^+} = \pm 1, \mp 1$. In case of the b quark study we have studied only the configuration $\mathcal{P}_{e^-}, \mathcal{P}_{e^+} = \mp 1$ since this study is just considered as a supporting study for the t quark analysis and the chosen polarisation configuration is the more challenging for the detector performance due to larger migration effects in the polar angle reconstruction.

More precisely the results presented in this note are based on the following samples:

- $e^+e^- \rightarrow t\bar{t}$:
 - $yyxye\nu, \mathcal{P}_{e^-}, \mathcal{P}_{e^+} = \mp 1$: <https://ild.ngt.ndu.ac.jp/elog/opt-data/?GenProcessID=108670>
This sample contains the final state resulting from the $W \rightarrow e\nu$ decay.
 - $yyxye\nu, \mathcal{P}_{e^-}, \mathcal{P}_{e^+} = \pm 1$: <https://ild.ngt.ndu.ac.jp/elog/opt-data/?GenProcessID=108670>
This sample contains the final state resulting from the $W \rightarrow e\nu$ decay.
 - $yyxyl\nu, \mathcal{P}_{e^-}, \mathcal{P}_{e^+} = \mp 1$: <https://ild.ngt.ndu.ac.jp/elog/opt-data/?GenProcessID=108675>.
This sample contains the final state resulting from the $W \rightarrow \ell\nu$ decay with $\ell = \mu, \tau$. For the analysis presented here the final state with $\ell = \tau$ has been discarded.
 - $yyxyl\nu, \mathcal{P}_{e^-}, \mathcal{P}_{e^+} = \pm 1$: <https://ild.ngt.ndu.ac.jp/elog/opt-data/?GenProcessID=108676>.
This sample contains the final state resulting from the $W \rightarrow \ell\nu$ decay with $\ell = \mu, \tau$. For the analysis presented here the final state with $\ell = \tau$ has been discarded.
- $e^+e^- \rightarrow b\bar{b}$: The $b\bar{b}$ events are extracted from a sample of simulated $q\bar{q}$ events <https://ild.ngt.ndu.ac.jp/elog/opt-data/?GenProcessID=250114> with $q = u, d, s, c, b$. The generated cross section for these events is 32470 fb and the total integrated luminosity is about 46 fb $^{-1}$. The genuine $e^+e^- \rightarrow b\bar{b}$ at 500 GeV is about 4% of the total cross section yielding a total number of events of about 60000.

Note that the analysis of the $e_R^+e_L^- \rightarrow t\bar{t}$ came quite late in the study since it is generally considered that the (semi-leptonic) $e_L^+e_R^- \rightarrow t\bar{t}$ is the more challenging channel. Therefore, the corresponding control plots in Secs. 3 and 4.2 are only given for this channel in this note.

3. Efficiencies and Control plots

Figure 1 demonstrates that the studies presented in this note test the detector performance for very different momenta of the final state b quark.

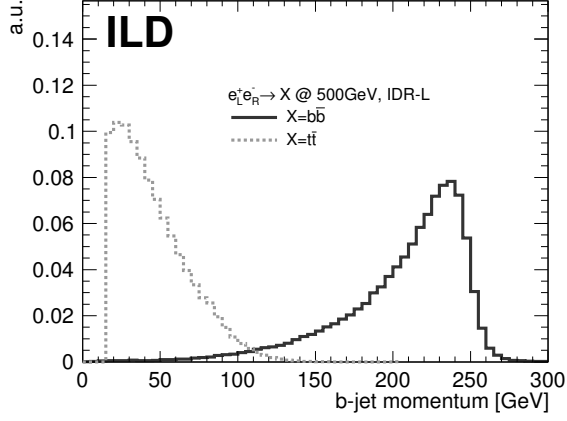


Figure 1: Momentum of the b -jet with cheated identification for $e^+e^- \rightarrow b\bar{b}$ and $e^+e^- \rightarrow t\bar{t}$ processes.

The Figs. 2 and 3 show the missed tracks before and after vertex recovery for the $e^+e^- \rightarrow b\bar{b}$ and $e^+e^- \rightarrow t\bar{t}$ analyses, respectively. Both figures suggest a systematic improvement in the assignment of secondary vertices.

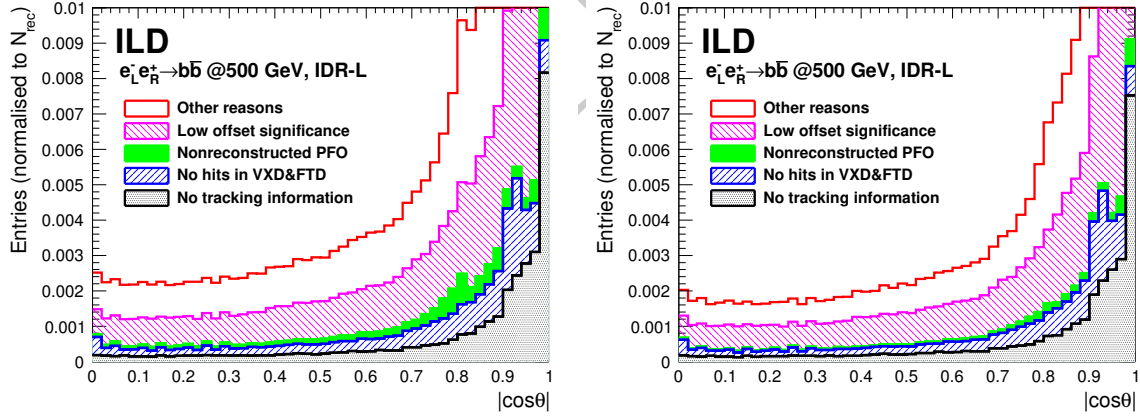


Figure 2: Polar angle of missed tracks before (left) and after (right) vertex recovery in case of the $e^+e^- \rightarrow b\bar{b}$ process.

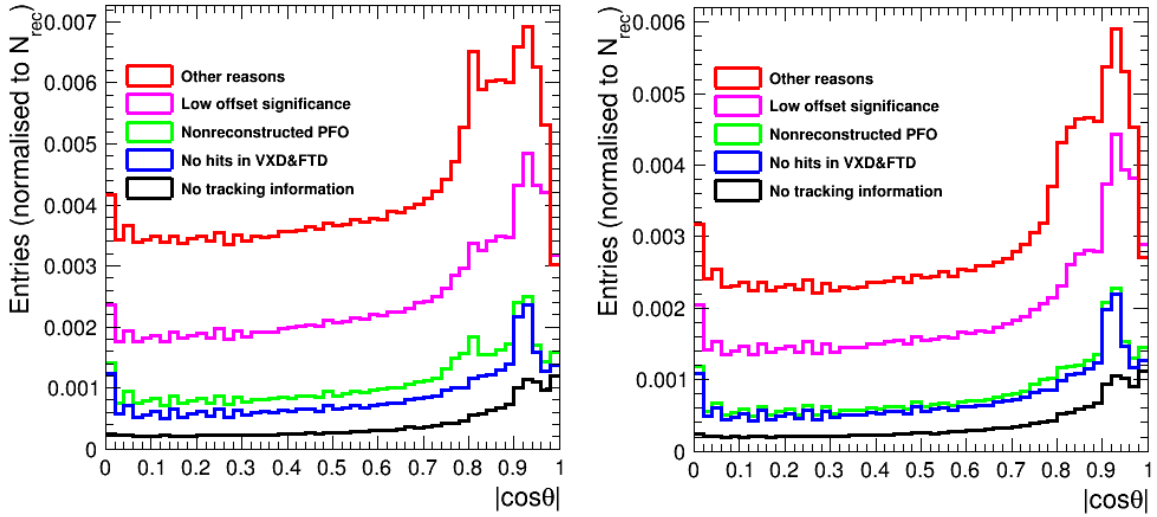


Figure 3: Polar angle of missed tracks before (left) and after (right) vertex recovery in case of the $e^+e^- \rightarrow t\bar{t}$ process. *DIFFERENT y-AXIS RANGES. DIFFERENT FILL STYLE COMPARED WITH Fig. 2.*

This improvement is quantified in Figs. 4 and 5 where the purity of the b -charge reconstruction is shown as a function of the b -tag value, the reconstructed b -momentum $|p_{had}|$ the number of reconstructed tracks assigned to a secondary vertex N_{rec} and finally the polar angle of the b -hadron. here denoted as $|\cos\theta|$. The b -charge purity is defined as

$$p_b = N_{correct}/N_{jet,tot}. \quad (4)$$

with $N_{correct}$ being the number of b -jets with correctly reconstructed b quark charge. This value normalised to the total number of b -jets $N_{b-jet,tot}$ for which a charge assignment according to e.g. Table 2 can be made.

The improvement is larger for the process $e^+e^- \rightarrow t\bar{t}$ than for $e^+e^- \rightarrow b\bar{b}$. Qualitatively this is expected since as a consequence of the different b -jet momenta, see Fig. 1, also the tracks produced in the decay of the b -hadron are softer in case of top-pair production. In case of $e^+e^- \rightarrow t\bar{t}$ the improvement is 10% over a large range in $|\cos\theta|$ and mainly driven by three to five prong decays. Both results will further improve once the vertex recovery takes also the impact parameter z_0 into account. All results shown so far in this section have been obtained for the large detector model. The conclusions for the small detector model are similar.

The lower right panels of Figs. 4 and 5 show a drop in purity for large values of $|\cos\theta|$. This is compatible with the drop in acceptance that is shown in Fig. 6 for the case $e^+e^- \rightarrow b\bar{b}$ as a function of the polar angle of the reconstructed b -jet $|\cos\theta_b|$. Within statistical errors the results are the same for the large and the small detector model. However, towards large values of $|\cos\theta_b|$ the large detector performs systematically better than the small detector.

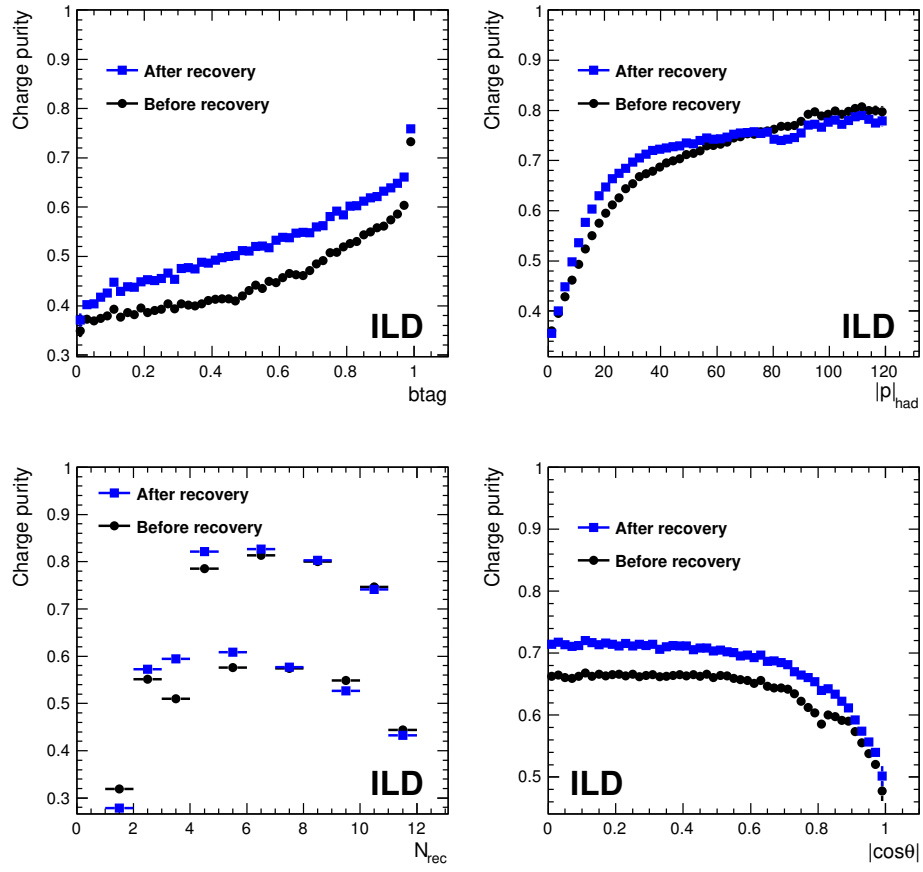


Figure 4: Purity before and after vertex recovery in case of the $e^+e^- \rightarrow t\bar{t}$ process for different observables. *PROPOSE TO CHANGE $|\cos\theta|$ to $|\cos\theta_B|$ TO INDICATE THAT IT IS THE B-HADRON*

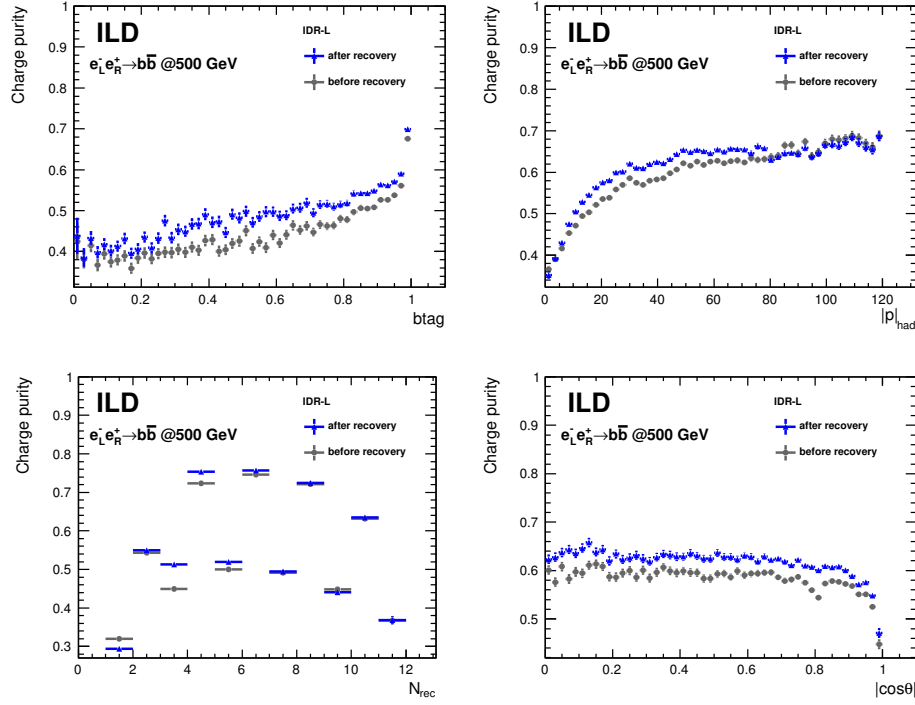


Figure 5: Purity before and after vertex recovery in case of the $e^+e^- \rightarrow t\bar{t}$ process for different observables. *PROPOSE TO CHANGE $|\cos \theta|$ to $|\cos \theta_B|$ TO INDICATE THAT IT IS THE B-HADRON*

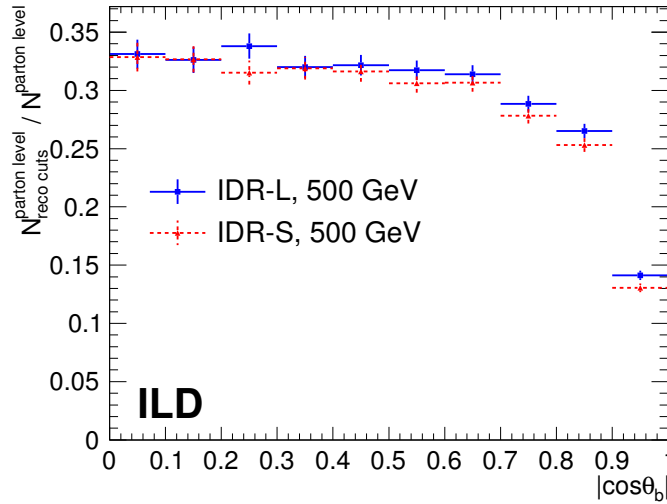


Figure 6: Detector acceptance distribution for b-tagged jets. Note the figure shows the acceptance after the full selection given in Tab. 1.

146 A component that distinguishes the ILD Detector from other proposals for e^+e^- colliders is the TPC
 147 as the central tracking system. Beside the precise momentum measurement the dE/dx measurement
 148 in the gaseous medium allows for a particle identification. Since around 87% of B-Mesons (neutral or

charged) contain a charged Kaon among their decay products the particle ID can support greatly the charge determination of the b quark.

The left part of Fig. 7 shows the dE/dx values obtained in simulation for different particle types as a function of the particle momentum. The lines indicate a strip with an accumulation of signals produced by Kaons. A minimum momentum of 2 GeV is required for the selection of Kaons. The right part of Fig. 7 shows the variation of the purity as a function of the Kaon selection efficiency that corresponds to a variation of the width of the strip in the previous figure. A closer look into the separation power in different momentum ranges is given in App. A.

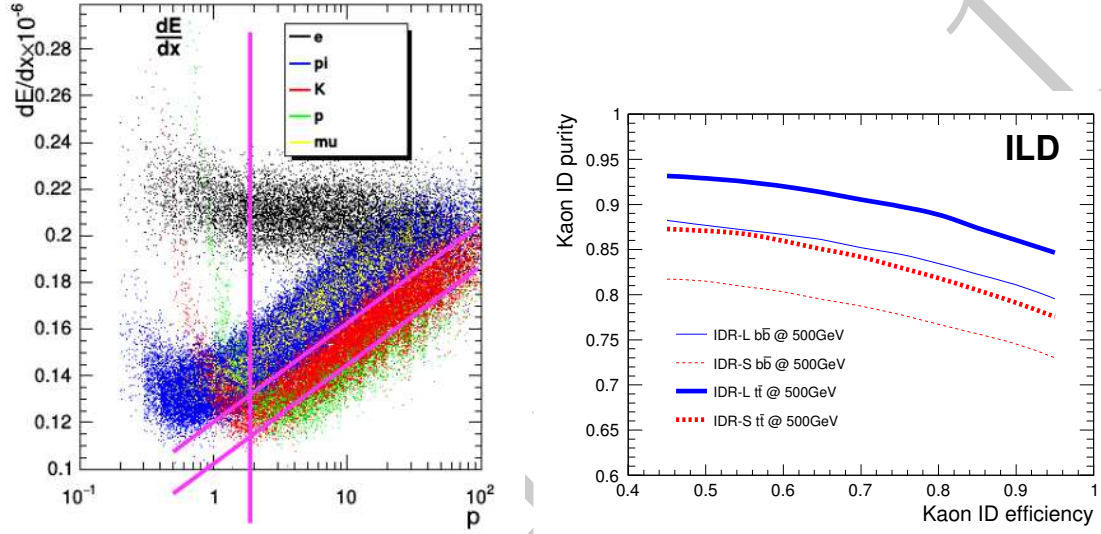


Figure 7: Left: Simulated dE/dx spectrum for different particle types. The lines indicate the cuts for the Kaon selection. Right: Purity of the Kaon selection as a function of the Kaon selection efficiency.

4. Event selection

In the following the event selection of the two final states under study will be presented. The different complexities of the final states require different set of cuts. The t quark is composed from its decay products, the b quark and the W boson and the final state le

4.1. Analysis details specific to the $e_L^- e_R^+ \rightarrow b\bar{b}$ analysis

Table 1 shows the selection efficiencies for the $e_L^- e_R^+ \rightarrow b\bar{b}$ analysis. In this case events that are subject to the radiative return to the Z , implying an energetic final state photon, have to be suppressed. Therefore cuts on the sum of the masses of the two jets and a cut on the photon energy are introduced. The overall efficiency after selection of events with consistent b quark charge is with around 28% to 29% similar for both detector models. For the b -charge measurement opposite charges in opposite jets are required. The charges are either derived from the tracks pointing to the secondary vertex or from the Kaon charge or from a combination of both. An event is selected if there is one combination with a consistent result. The efficiencies for the different methods are given in Tab. 2. The purity of the different methods is shown in Fig. 8. In both cases there is no large difference between the two detector models although the large detector seems to perform slightly better for the double Kaon method. This suggests that the smaller outer radius of the TPC puts a, however minor, on the dE/dx measurement.

$$e_L^- e_R^+ \rightarrow b\bar{b} \text{ at } 500 \text{ GeV}$$

	IDR-L			IDR-S		
	Signal	B _{q\bar{q}} /S	B _{rad.Z} /S	Signal	B _{q\bar{q}} /S	B _{rad.Z} /S
Full sample	100.0%	1800.5%	359.1%	100.0%	1800.6%	359.0%
$b_{tag}(jet_1) > 0.9$ and $b_{tag}(jet_2) > 0.2$	70.2%	2.3%	147.7%	69.9%	2.3%	149.0%
$m_{jet_1+jet_2} > 200 GeV$	68.2%	1.4%	6.7%	67.8%	1.2%	6.7%
$E_{photon} < 100 GeV$	64.8%	1.3%	1.7%	64.3%	1.2%	1.6%
double jet-charge measurement	28.9%	1.0%	1.0%	27.9%	0.9%	1.0%

Table 1: Selection efficiency and B/S rejection for some bkg sources

$$e_L^- e_R^+ \rightarrow b\bar{b} \text{ at } 500 \text{ GeV}$$

	IDR-L	IDR-S
$Vtx+Vtx$	12.9%	12.8%
$K+K$	4.4%	4.0%
$Vtx+K$ (diff. jets)	3.9%	3.7%
$Vtx+K$ (same jet)	7.7%	7.4%

Table 2: Final selection efficiency, after double jet-charge measurement

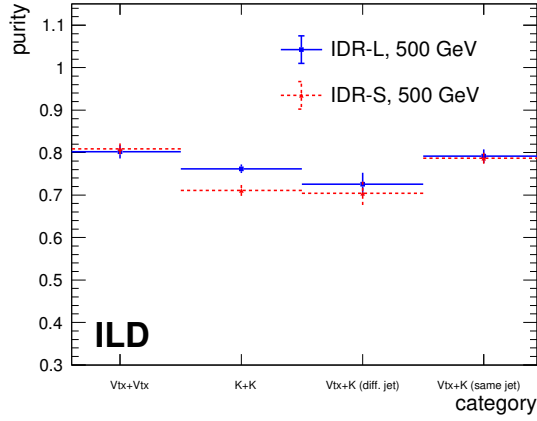


Figure 8: Purity of the methods listed in Tab. 2 used for the reconstruction of the vertex charge in the $e_L^- e_R^+ \rightarrow b\bar{b}$.

174 4.2. Analysis details specific to the $e^+e^- \rightarrow t\bar{t}$ analysis

175 The t quark is composed from its decay products, the b quark and the W boson and the charge of
 176 the lepton is a measure to distinguish the t from the \bar{t} quark.

177 Figure 9 shows in the left panel the energy distribution of the isolated lepton in the laboratory
 178 frame. The distribution features a maximum at around 30 GeV and a tail towards higher energies. The
 179 right panel shows the polar angle spectrum of the isolated lepton. The distribution decreases slightly
 180 with a sharp drop at the acceptance limit of the detector. The distribution reveals also acceptance
 181 drops at $\cos\theta_\ell = 0$ and $\cos\theta_\ell = 0.8$ that correspond to the position of the TPC anode plate and the
 182 barrel-endcap transition region, respectively.

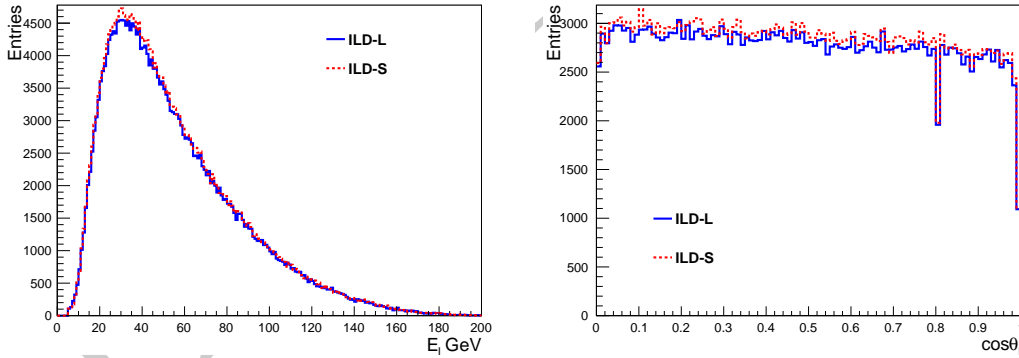


Figure 9: Left: Energy of the isolated lepton in $e_L^+ + e_R^- \rightarrow t\bar{t}$. Right: Polar angle distribution of the isolated lepton in $e_L^+ e_R^- \rightarrow t\bar{t}$.

183 For completeness Fig. 10 shows the mass distribution of the hadronic W and the hadronic t quark.

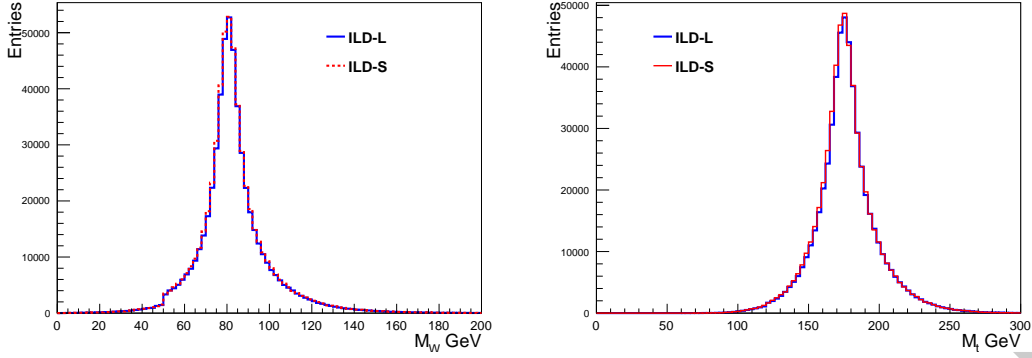


Figure 10: Left: Mass distribution of the hadronic W in $e_L^+ e_R^- \rightarrow t\bar{t}$. Right: Mass distribution of the hadronic t quark in $e_L^+ e_R^- \rightarrow t\bar{t}$.

Tables 3 and 5 give the efficiencies after each cut applied for the selection of $t\bar{t}$ events. The first part lists *General selection cuts* that were already used in Ref. [5].

The polar angle of the t quark $\cos\theta_t$ is reconstructed from the hadronically decaying t quark. For the polar angle spectrum the charge of the t quark has to be determined and the b quark and the W -boson have to be correctly associated. This is more involved in the $e_L^- e_R^+ \rightarrow t\bar{t}$ case than in the $e_R^- e_L^+ \rightarrow t\bar{t}$ case due to the different kinematics provoked by the $V - A$ interaction of the t quark decay. The different steps for an accurate reconstruction of the polar angle spectrum are listed in the following¹.

- In a first step further cuts on the sum of the Lorentz factor of the two tops of $\gamma_t^{had} + \gamma_t^\ell > 2.4$ is applied. Here γ_t^{had} is the Lorentz factor of the hadronically decaying t quark and γ_t^ℓ the Lorentz factor of the leptonically decaying t quark. In case of $e_L^- e_R^+ \rightarrow t\bar{t}$ a cut on the B -hadron momentum of $p_{B,had.} > 15$ GeV is applied in addition.
- The semi-leptonic decay of the t quark gives powerful information for the event reconstruction giving rise to the variable L_{cut} , which means the charge of the isolated lepton plus a cut on the event quality of $\chi^2 < 15$ that is motivated in Ref. [5].
- For the b quark charge determination the used methods are very much similar to those in 2. The vertex charge is supported by the requirements of $btag > 0.8$ and a minimal hadron momentum of 25 GeV as motivated in Ref. [6]².
- The various methods of measuring the b quark charge are also combined with the charge of the isolated lepton L . In this case an additional cut on $\gamma_t^{had} > 1.23$ is applied.
- The final decision on the t quark charge is obtained from the sum of the charges associated to the different methods. If the sum is smaller (greater) than zero then the hadronically decaying t quark candidate is said to be the t quark (\bar{t} quark).

Table 3 gives the final selection efficiency for the case $e_L^- e_R^+ \rightarrow t\bar{t}$ after the inclusion of the respective cuts. Table 4 shows the efficiencies after application of the various methods described in the list of items above. The addition of methods other than L_{cut} increases the efficiency by around 38%. Figure 11 shows for completeness the purity of the selection for those cases in which the information from the t

¹We are aware that the set of cuts does not look straight forward and needs revision in the Post-IDR phase.

²In the $e^+e^- \rightarrow b\bar{b}$ analysis this additional requirement was removed. It would have to be investigated whether this requirement can be omitted in case of $e_L^- e_R^+ \rightarrow t\bar{t}$, too

$$e_L^- e_R^+ \rightarrow t\bar{t} \text{ at } 500 \text{ GeV}$$

General selection cuts	IDR-L	IDR-S
Isolated Lepton	92.1%	92.1%
$btag_1 > 0.8$ or $btag_2 > 0.3$	81.2%	81.1%
Thrust < 0.9	81.2%	81.1%
Hadronic mass	78.2%	78.2%
Reconstructed m_W and m_t	73.4%	73.4%
t quark polar angle spectrum		
$\gamma_t^{had.} + \gamma_t^\ell > 2.4$	62.2%	xx%
$ p_{B,had} > 15 \text{ GeV}$	34.5%	xx%
" $t\bar{t}$ identification"	30.6%	30.5%
b quark polar angle spectrum		
No additional cuts		

Table 3: Event selection efficiencies after preselection and reconstruction of the polar angle spectrum of the t quark and that of the underlying b quark.

Methods	IDR-L	IDR-S
L_{cut}	22.1%	xx%
$L+Vtx$	28.6%	xx%
$L+K$	29.6%	xx%
$Vtx+Vtx$	30.1%	xx%
$K+K$	30.3%	xx%
$Vtx+K$ (same jet)	30.5%	xx%
$Vtx+K$ (different jet)	30.6%	xx%

Table 4: Efficiency increase after the progressive application of the various methods introduced to ensure a correct association of the W boson and the b quark in case of $e_L^- e_R^+ \rightarrow t\bar{t}$. The last line of this table corresponds to the line " $t\bar{t}$ identification" in Tab. 3.

quark and the \bar{t} quark decay have been combined. As in case of $e^+e^- \rightarrow b\bar{b}$ differences between the large and the small detector are observed for those combinations that include Kaons with the biggest difference for the pure Kaon combination $K+K$. The Kaon measurement is the domain of the TPC and the both models feature different outer TPC radii.

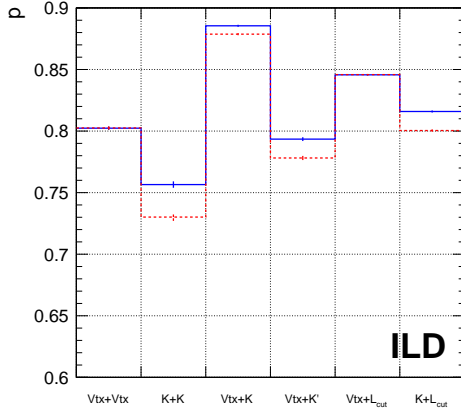


Figure 11: Purities of the various combinations to determine the charge of the t and the \bar{t} quark. **STILL NOT SAME STYLE AS FIG. 8**

$$e_R^- e_L^+ \rightarrow t\bar{t} \text{ at } 500 \text{ GeV}$$

General selection cuts	IDR-L	IDR-S
Isolated Lepton	94.1%	94.0%
$btag_1 > 0.8$ or $btag_2 > 0.3$	84.9%	84.8%
Thrust < 0.9	84.9%	84.8%
Hadronic mass	82.2%	82.3%
Reconstructed m_W and m_t	77.6%	77.5%
t quark polar angle spectrum		
$\gamma_t^{had.} + \gamma_t^\ell > 2.4$	64.1%	64.1%
b quark polar angle spectrum		
vertex charge	10.8%	10.3%

Table 5: See Tab. 3 for details.

Table 5 shows the selection efficiencies for the case $e_R^- e_L^+ \rightarrow t\bar{t}$. The cut scenario for the reconstruction of the polar angle of the t quark is much simpler than in case of $e_L^- e_R^+ \rightarrow t\bar{t}$. The reason is that the t quark direction is in first approach given by the W boson such that a wrong association of W boson and b quark doesn't alter the t quark direction. For the polar angle spectrum of the underlying b quark the analysis is restricted to the the combination of the vertex charge. This is further discussed in Sec. 5.

5. Results

Figure 12 shows the spectrum of the polar angle $\cos \theta_b$ after the selection given in Tabs. 1 and 2 and the application of Eq. 3 for $e_L^- e_R^+ \rightarrow b\bar{b}$. Large and small detector agree within statistical uncertainties. It seems however that there is larger migration for the small detector.

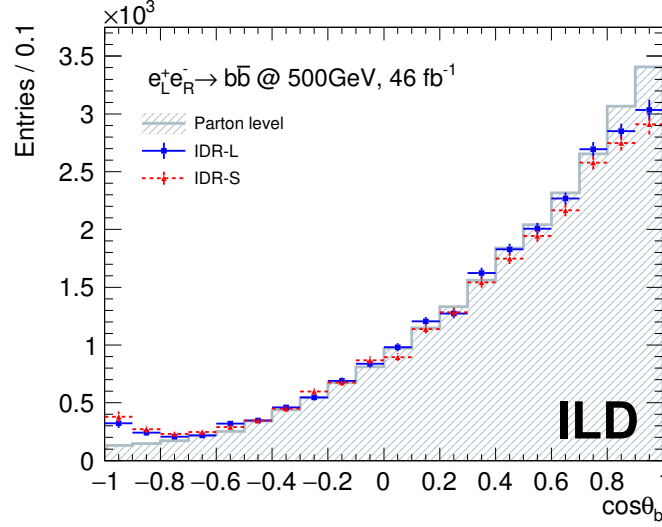


Figure 12

The left part of Fig. 13 shows the polar angle distribution of $t\bar{t}$ of the generated and reconstructed data for the large and the small detector models. For this all cuts and methods given in Tabs. 3 and 4 have been applied. The red dotted line shows the fitted result of the reconstructed events (WHAT ARE WE FITTING HERE?). The right part shows the polar angle distribution of the underlying b quark for the same set of cuts. The polar spectrum can be accurately reconstructed over the entire polar angle. Acceptance drops at large absolute values of the polar angle become visible in the polar angle spectrum of the b quark (In this case no attempt was made to correct for acceptance as in Fig. 12). However, in the range $-0.8 < \cos \theta_b < 0.8$ also the polar angle of the b quark can be accurately reconstructed.

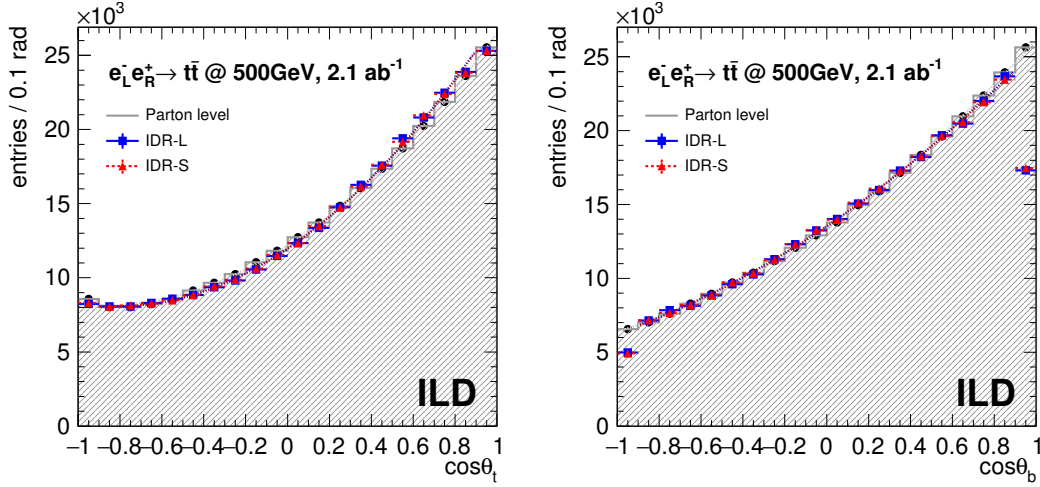


Figure 13: Results for $e_L^- e_R^+ \rightarrow t\bar{t}$ Left: Polar angle distribution for t quark. Right: Polar angle distribution for the b quark that is issue of the t quark decay. The distributions for IDR-S is normalised to the one for IDR-L so that both histograms will be on the same level. **y-AXIS LABEL IS WRONG! SHOULD BE Entries/0.1.**

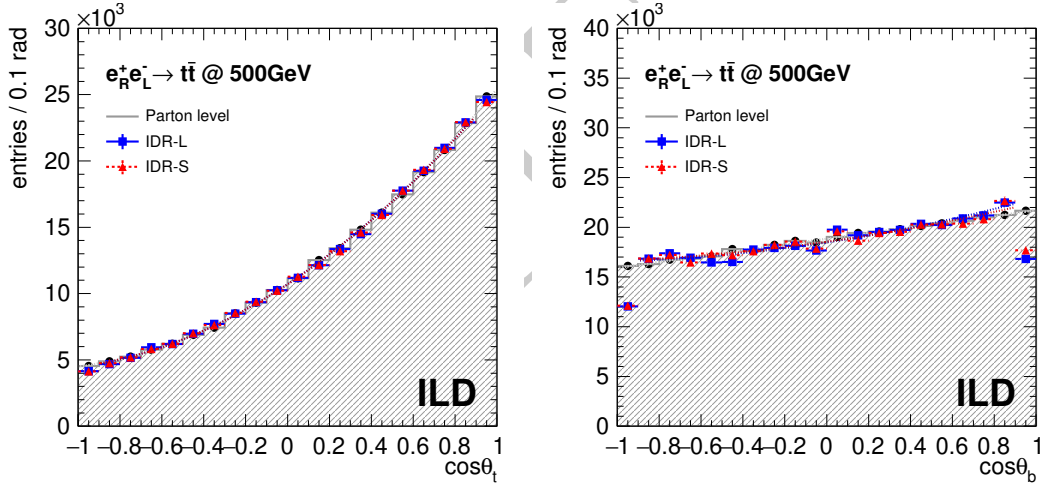


Figure 14: Same as Fig. 13 for $e_R^- e_L^+ \rightarrow t\bar{t}$. **y-AXIS LABEL IS WRONG! SHOULD BE Entries/0.1.**

The left part of Fig. 14 shows the polar angle spectrum for the case $e_R^- e_L^+ \rightarrow t\bar{t}$ after application of the cuts introduced in Tab. 5. The generated spectrum can be very precisely reconstructed. The right hand part of Fig. 14 shows the polar angle spectrum of the underlying b quark. Here only events with consistent vertex-charge measurements have been included. The polar angle of the b quark can also in this case be very well reconstructed. However, the efficiency drops to 10% as already quantified in the lower part of Tab. 5. The inclusion of the other methods is subject to further studies. Preliminary results show that taking into account the isolated lepton “swamps” the polar angle spectrum with events in which the b quark direction is not constrained. One reason is certainly that in the case of $e_R^- e_L^+ \rightarrow t\bar{t}$ the b quark is on average softer than in the case of $e_L^- e_R^+ \rightarrow t\bar{t}$.

Comparing the spectra of the underlying b quarks demonstrates more clearly than the actual t quark polar angle spectra the different polarisations of the t quarks projected out by the flight direction of the b quark. In case of $e_L^- e_R^+ \rightarrow t\bar{t}$ the final state is enriched with left-handed t quarks. In this case the

246 b quark is preferably emitted in the direction of the t quark. Therefore the two polar angle spectra in
 247 Fig. 13 look similar to each other. In case of $e_R^- e_L^+ \rightarrow t\bar{t}$ the final state is enriched with right-handed
 248 t quarks. In this case the b quark is preferable emitted opposite to the direction of the t -quark. The
 249 polar angle of the b quark is a consequence of the Jacobian peak in the vicinity of $\cos \theta_{Wb} = 0$, with
 250 $\cos \theta_{Wb}$ being the opening angle between the b quark and the W boson, generated by the boost of
 251 the back-to-back configuration in the centre-of-mass frame of the decaying t quark into the laboratory
 252 frame.

253 5.1. Interpretation of the results

254 Table 6 lists the generated and reconstructed value of the forward-backward asymmetry $A_{FB, reco}^t$
 255 as an estimator for the quality of the reconstruction.

	$e_L^- e_R^+ \rightarrow t\bar{t}$		$e_R^- e_L^+ \rightarrow t\bar{t}$	
	IDR-L	IDR-S	IDR-L	IDR-S
$A_{FB, gen}^t$	0.329		0.430	
$A_{FB, reco}^t$	0.342	0.340	0.430	0.430

Table 6: Selection efficiencies and resulting $A_{FB, reco}^t$ for both beam polarisations and the two detector models under study.

256 So far the results have been presented for full beam polarisation. Using the known formula [11]

$$\sigma_{\mathcal{P}_{e-}, \mathcal{P}_{e+}} = \frac{1}{4} [(1 - \mathcal{P}_{e-} \mathcal{P}_{e+})(\sigma_{-,+} + \sigma_{+,-}) + (\mathcal{P}_{e-} - \mathcal{P}_{e+})(\sigma_{+,-} - \sigma_{-,+})], \quad (5)$$

257 with $\sigma_{-,+}$ and $\sigma_{+,-}$ being the fully polarised cross-sections, the results can be extrapolated to the
 258 realistic beam polarisations of $\mathcal{P}_{e-}, \mathcal{P}_{e+} = \mp 0.8, \pm 0.3$. The resulting Born level cross sections are
 259 1070 fb^{-1} in case of $\mathcal{P}_{e-}, \mathcal{P}_{e+} = -0.8, +0.3$ and 519 fb^{-1} in case of $\mathcal{P}_{e-}, \mathcal{P}_{e+} = +0.8, -0.3$. The
 260 resulting statistical errors for an integrated luminosity of $\mathcal{L} = 1600 \text{ fb}^{-1}$ at each of the two polarisation
 261 settings are given in Table 7.

	$\mathcal{P}_{e-}, \mathcal{P}_{e+}$	$(\delta\sigma/\sigma)_{stat.} [\%]$	$(\delta A_{FB}^t/A_{FB}^t)_{stat.} [\%]$
IDR-L	$-0.8, +0.3$	0.17	0.7
	$+0.8, -0.3$	0.25	0.53
IDR-S	$-0.8, +0.3$	0.17	0.7
	$+0.8, -0.3$	0.25	0.53

Table 7: Statistical precisions expected for the cross sections and A_{FB}^t for the case $\mathcal{P}_{e-}, \mathcal{P}_{e+} = -0.8, +0.3$ and the two detector models under study.

262 For both, the cross section and the forward backward asymmetry it can be expected that even at
 263 full luminosity the statistical error has to be taken into account. However, the systematic errors need
 264 to be carefully estimated. For the present analysis it would have to be checked how much the sample
 265 is contaminated by events for which the semi-leptonic decay yields τ -leptons or the τ -leptons are taken
 266 into account as in [5]. The contamination by fully hadronic $t\bar{t}$ events can be expected to be small.

267 To put the results into context, the precisions on the cross-sections and the forward-backward
 268 asymmetries are translated into precisions on electromagnetic form factors of the t quark. Figure 15
 269 shows the precisions at the 1σ level expected at ILC500. The precisions are compared with those
 270 expected after the full HL-LHC running and estimations produced for FCC-ee [12] at the same confi-
 271 dence level. For ILC500, the two sets F_1 and F_2 have been extracted separately but within each set
 272 the uncertainties have been extracted simultaneously. The projections for HL-LHC are derived from
 273 the *individual* constraints of EFT Wilson coefficients presented in Tab.C2.3 of Ref. [13] (the most

274 favorable scenario for HL-LHC). These figures demonstrate clearly the superiority of a linear e^+e^-
 275 collider with polarised beams operated at an adequate centre-of-mass energy.

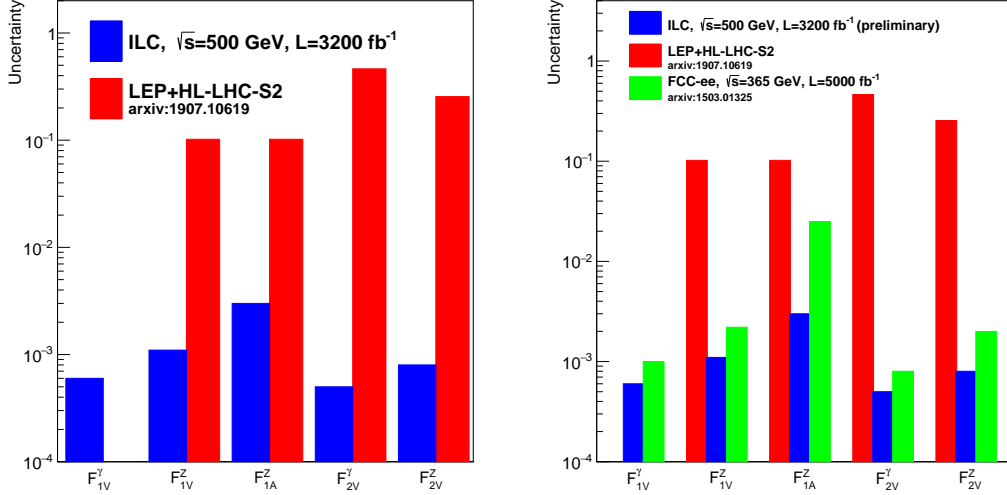


Figure 15: Precisions the on electromagnetic t quark form factors expected after ILC500 compared with those expected after the full HL-LHC running and an estimation for FCC-ee after 5000 fb⁻¹. The EFT does not include operators that map onto the F_{11}^t form factor. See text for further details.

276 6. Summary

277 This note presents a study of the processes $e^+e^- \rightarrow t\bar{t}$ and $e^+e^- \rightarrow b\bar{b}$ in $epem$ collisions with
 278 polarised beams at $\sqrt{s} = 500$ GeV. The events are simulated and reconstructed with the large and the
 279 small models of the ILD detector.

280 In case of t quark pair production the analysis focus on the semi-leptonic decay channel in which
 281 the isolated lepton is available for the distinction between the t quark and the \bar{t} quark. In case of
 282 the $e^+e^- \rightarrow b\bar{b}$ process the distinction has to be made by the measurement of the b quark charge,
 283 which helps also for a proper reconstruction of the $t\bar{t}$ quark pair. The charge of the b quark can be
 284 reconstructed with a purity of 80% using the combination of information available from the vertex
 285 charge, Kaons that have been measured in the TPC of ILD or isolated leptons in case of t -quark
 286 production.

287 The analysis shows that both, the large and the small detector model, are capable to provide
 288 a high precision measurement of the cross-section and the polar angle spectrum of semi-leptonic $t\bar{t}$
 289 events with a mild advantage for the large detector. Assuming a total intergrated luminosity of
 290 $\mathcal{L} = 3200 \text{ fb}^{-1}$ shared equally between the beam polarisations $\mathcal{P}_{e^-}, \mathcal{P}_{e^+} = \mp 0.8, \pm 0.3$ the cross sections
 291 of $t\bar{t}$ production can be measured to a statistical precision of about 0.2% and the forward backward
 292 asymmetry to a statistical precision of around 0.6%. The statistical precision on the cross section and
 293 the forward backward asymmetries are compatible with the scaling of the results found in [5].

294 For the first time the polar angle spectrum of the underlying b quark, issue of the t quark decay,
 295 is presented. This spectrum reveals more clearly the acceptance drop towards large polar angles. Still
 296 the polar angle of the b quark can be reconstructed accurately within $\cos\theta < 0.8$ for the two studied
 297 beam polarisation $\mathcal{P}_{e^-}, \mathcal{P}_{e^+} = \pm 1, \mp 1$. In case $\mathcal{P}_{e^-}, \mathcal{P}_{e^+} = +1, -1$ the efficiency drops however to
 298 10% (compared with 30% for the case $\mathcal{P}_{e^-}, \mathcal{P}_{e^+} = +1, -1$). Here further work is clearly needed to
 299 improve the event yield. Both results allow however already now for the perspective that in the future

the fully hadronic final state can be taken into account for the analysis and that observables specific to the produced b quark can be addressed.

The study of the $t\bar{t}$ production has been accompanied by the second benchmark study $e^+e^- \rightarrow b\bar{b}$. Since only 46 fb^{-1} are available for this channel it should be rather considered as an auxiliary study. However, it is shown that the polar angle spectrum can be very well reconstructed even for the hard b -jets and that migrations can be controlled at a satisfactory level. It is therefore justified to conclude that ILD should be able to make precision measurements of this channel even at a centre-of-mass energy of 500 GeV. Although the results are similar for both the small and the large detector model, this analysis, more than the analysis of the $t\bar{t}$ process reveals a slight preference for the large model. This is most clearly visible in the purity of the charge measurement using Kaons, which may depend on the actual TPC radius.

Also in the future all heavy quark studies should be carried out in close cooperation with each other. As can be seen from the present study there are many common issues between the studies. In the future emphasis will be put on systematic uncertainties given e.g. by hemisphere correlations. These studies may be more involved in case of $t\bar{t}$ since the two b quarks are in general not back-to-back.

Acknowledgements

References

- [1] F. Richard, “Present and future constraints on top EW couplings”, LAL-ORSAY-14-55, [arXiv:1403.2893 \[hep-ph\]](#).
- [2] L. Randall and R. Sundrum, “A Large mass hierarchy from a small extra dimension”, *Phys.Rev.Lett.* **83** (1999) 3370–3373, MIT-CTP-2860, PUPT-1860, BUHEP-99-9, [arXiv:hep-ph/9905221 \[hep-ph\]](#).
- [3] A. Djouadi, G. Moreau, and F. Richard, “Resolving the A(FB)**b puzzle in an extra dimensional model with an extended gauge structure”, *Nucl.Phys.* **B773** (2007) 43–64, LPT-ORSAY-06-060, LAL-ORSAY-06-144, [arXiv:hep-ph/0610173 \[hep-ph\]](#).
- [4] G. Durieux and O. Matsedonskyi, “The top-quark window on compositeness at future lepton colliders”, *JHEP* **01** (2019) 072, DESY 18-114, DESY-18-114, [arXiv:1807.10273 \[hep-ph\]](#).
- [5] M. S. Amjad *et al.*, “A precise characterisation of the top quark electro-weak vertices at the ILC”, *Eur. Phys. J.* **C75** (2015) no. 10, 512, IFIC-15-15, LAL-15-111, [arXiv:1505.06020 \[hep-ex\]](#).
- [6] S. Bilokin, R. Pöschl, and F. Richard, “Measurement of b quark EW couplings at ILC”, LAL-17-052, [arXiv:1709.04289 \[hep-ex\]](#).
- [7] S. Bilokin, *Hadronic showers in a highly granular silicon-tungsten calorimeter and production of bottom and top quarks at the ILC*. Theses, Paris Saclay, July, 2017. <https://tel.archives-ouvertes.fr/tel-01826535>.
- [8] T. Behnke, J. E. Brau, P. N. Burrows, J. Fuster, M. Peskin, *et al.*, “The International Linear Collider Technical Design Report - Volume 4: Detectors”, ILC-REPORT-2013-040, ANL-HEP-TR-13-20, BNL-100603-2013-IR, IRFU-13-59, CERN-ATS-2013-037, COCKCROFT-13-10, CLNS-13-2085, DESY-13-062, FERMILAB-TM-2554, IHEP-AC-ILC-2013-001, INFN-13-04-LNF, JAI-2013-001, JINR-E9-2013-35, JLAB-R-2013-01, KEK-REPORT-2013-1, KNU-CHEP-ILC-2013-1, LLNL-TR-635539, SLAC-R-1004, ILC-HIGRADE-REPORT-2013-003, [arXiv:1306.6329 \[physics.ins-det\]](#). %%CITATION = ARXIV:1306.6329;%%.
- [9] C. Adolphsen, M. Barone, B. Barish, K. Buesser, P. Burrows, J. Carwardine, J. Clark, H. Mainaud Durand, G. Dugan, E. Elsen, *et al.*, “The International Linear Collider Technical Design Report - Volume 3.II: Accelerator Baseline Design”, ILC-REPORT-2013-040, ANL-HEP-TR-13-20, BNL-100603-2013-IR, IRFU-13-59, CERN-ATS-2013-037, COCKCROFT-13-10, CLNS-13-2085, DESY-13-062, FERMILAB-TM-2554, IHEP-AC-ILC-2013-001, INFN-13-04-LNF, JAI-2013-001, JINR-E9-2013-35, JLAB-R-2013-01, KEK-REPORT-2013-1, KNU-CHEP-ILC-2013-1, LLNL-TR-635539, SLAC-R-1004, ILC-HIGRADE-REPORT-2013-003, [arXiv:1306.6328 \[physics.acc-ph\]](#).
- [10] T. Barklow, J. Brau, K. Fujii, J. Gao, J. List, N. Walker, and K. Yokoya, “ILC Operating Scenarios”, ILC-NOTE-2015-068, DESY-15-102, IHEP-AC-2015-002, KEK-PREPRINT -2015-17, SLAC-PUB-16309, [arXiv:1506.07830 \[hep-ex\]](#).

- [11] G. Moortgat-Pick, T. Abe, G. Alexander, B. Ananthanarayan, A. Babich, *et al.*, “The Role of polarized positrons and electrons in revealing fundamental interactions at the linear collider”, *Phys.Rept.* **460** (2008) 131–243, CERN-PH-TH-2005-036, DCPT-04-100, DESY-05-059, FERMILAB-PUB-05-060-T, IPPP-04-50, KEK-2005-16, PRL-TH-05-01, SHEP-05-03, SLAC-PUB-11087, [arXiv:hep-ph/0507011](#) [hep-ph].
- [12] P. Janot, “Top-quark electroweak couplings at the FCC-ee”, *JHEP* **04** (2015) 182, [arXiv:1503.01325](#) [hep-ph].
- [13] G. Durieux, A. Irls, V. Miralles, A. Peñuelas, R. Pöschl, M. Perelló, and M. Vos, “The electro-weak couplings of the top and bottom quarks – global fit and future prospects”, [arXiv:1907.10619](#) [hep-ph].

A. Details on particle separation via dE/dx

The Fig. 16 displays the normalised dE/dx spectrum for different particles in different momentum ranges for the large and the small detector model. In both cases there is a clear separation of Kaons from pions. The latter are however much more abundant. There is only a small population of protons. Figure 17 shows the dE/dx spectra for the two processes under study.

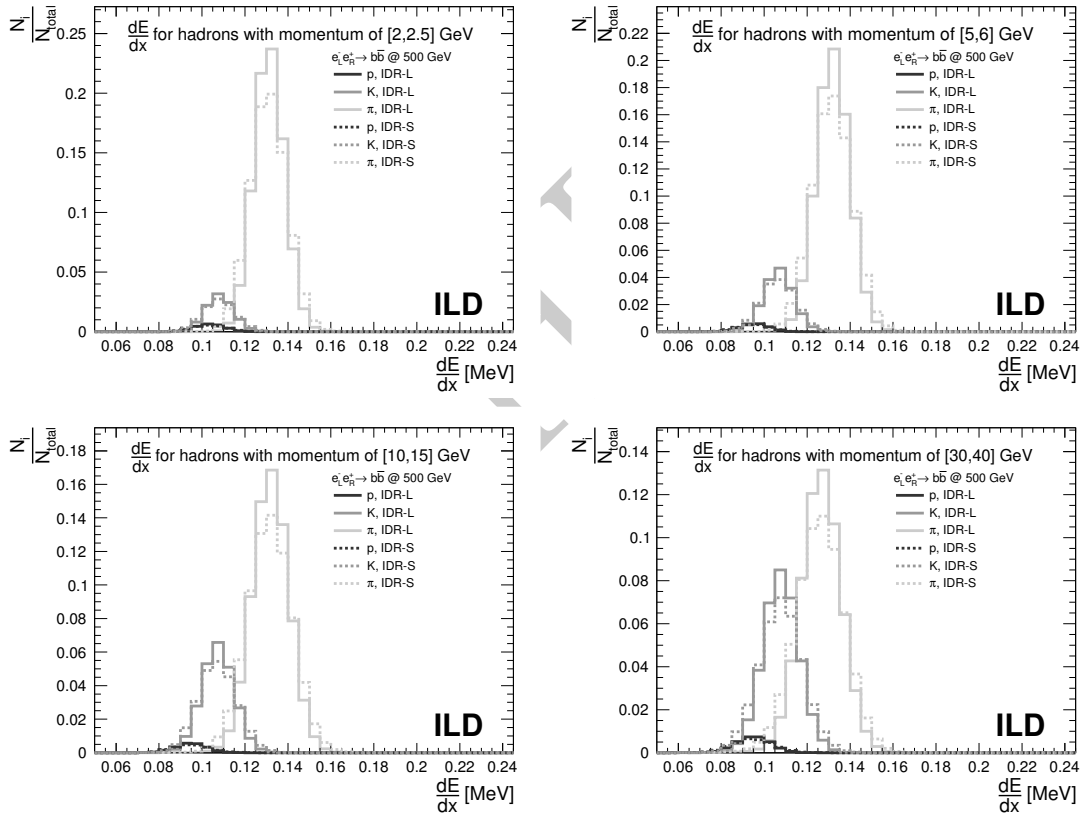


Figure 16: Projection of dE/dx for several momentum ranges. Comparison of hadron separation performance by different detector models in $b\bar{b}$ final states.

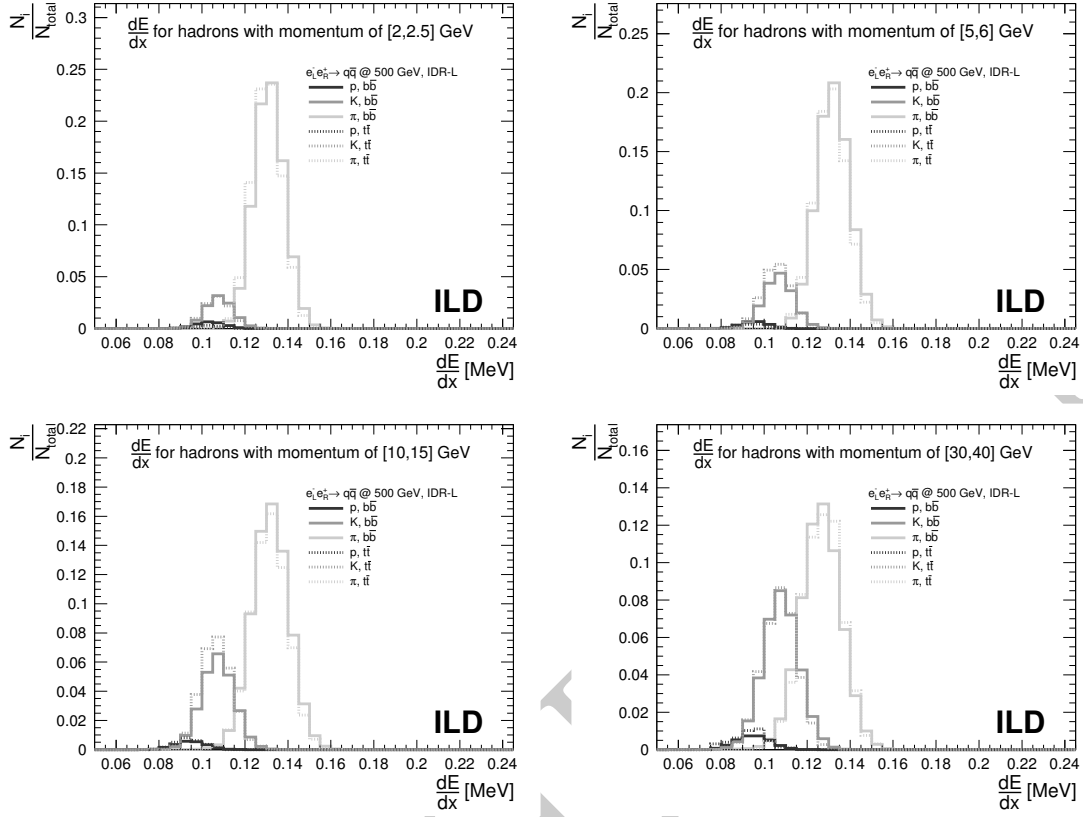


Figure 17: Projection of dE/dx for several momentum ranges. Comparison of hadron separation performance by the large model for different topologies.